J Mater Sci (2016) 51:9613–9624

Synthesis, growth mechanism, and photoluminescence property of hierarchical SnO_2 nanoflower-rod arrays: an experimental and first principles study

Manzhang Xu[1], Xiongfei Ruan[1], Junfeng Yan[1,*], Zhiyong Zhang[1,*], Jiangni Yun[1], Wu Zhao[1], Ting Li[1], and Yufei Shi[1]

[1] School of Information Science and Technology, Northwest University, Xi'an 710069, People's Republic of China

Received: 5 April 2016
Accepted: 22 June 2016
Published online: 27 July 2016

ABSTRACT

Upstanding SnO_2 nanorod arrays covered by hierarchical SnO_2 nanoflowers grow on the indium tin oxide (ITO) substrate through a direct hydrothermal method. Corresponding growth mechanism has been investigated along with the reaction time. The ITO substrate plays a role of seed layer and guides the nucleation of SnO_2 nanoflower-rod arrays (NFRAs), which promotes the SnO_2 crystal nucleation grow into nanorod arrays in the hydrothermal reaction. The photoluminescence (PL) spectrum of the obtained SnO_2 NFRAs architecture reveals that the oxygen vacancies (V_O) are major reasons of luminescence. In order to better understand the relationship between the V_O and the luminous mechanism, a first principles study is carried out. The calculation results based on the density functional theory (DFT) indicate the energy level of V_O with the three types of charge state (the ionization energy of the V_O^0 state, V_O^+ state, and V_O^{2+} state in band gap are 0.15, 2.84, and 3.15 eV, respectively) in SnO_2 NFRAs architecture, which is in agreement with the PL spectrum.

Introduction

Being a wide direct band gap semiconductor, SnO_2 is well known as one of the most promising functional nanostructure materials due to its wide energy gap (3.6 eV) and large binding energy (130 meV) at room temperature. SnO_2 has been extensively used as solar cells, sensors, and optoelectronics devices due to its excellent optical and electric properties [1–7]. Therefore, various SnO_2 nanostructures such as nanorods, nanowires, nanoflowers, and nanoarrays have been synthesized for the device [8–14]. Among these shapes, hierarchical nanostructure has attracted significant interest because of its widespread potential applications in many areas such as photodetectors and sensors [15–17]. The various morphologies of SnO_2 hierarchical nanostructure are usually synthesized by the hydrothermal method, which is highly praised by many researchers for its low cost, environmental friendship, and convenient synthesis. The size and morphology of these SnO_2 hierarchical

Address correspondence to E-mails: yanjf@nwu.edu.cn; zhangzy@nwu.edu.cn

DOI 10.1007/s10853-016-0169-0

nanostructures could be controlled by changing various reaction parameters, such as the reaction temperature, time, surfactant, and material source [18–26]. However, there are few literatures reported on synthesis SnO_2 nanoflower-rod arrays (NFRAs) architecture. Furthermore, most of the mechanisms of SnO_2 luminescence property mainly focus on the defects or band edge emission. In addition, the index of emission peaks both in the ultraviolet and visible emission region of SnO_2 is still a challenge. Therefore, in this work, a hierarchical SnO_2 NFRAs architecture was synthesized through a simple template-free hydrothermal process on the indium tin oxide (ITO) substrate. Moreover, a reasonable growth mechanism of the hierarchical SnO_2 NFRAs architecture was proposed based on the morphology and structure characterizations. In addition, corresponding photoluminescence (PL) property was investigated with a first principles study. The luminous mechanism was demonstrated based on the density functional theory (DFT) calculation. This research of SnO_2 material not only presents a way to synthesize the novel nanostructures but also provides theoretical reference of potential PL application.

Materials and methods

Materials synthesis

In a typical procedure, 0.3966 g $SnCl_4{\cdot}5H_2O$ (99 %) and 0.4667 g NaOH (99 %) were dissolved into deionized water, respectively, and the NaOH solution was added into $SnCl_4$ solution drop by drop. After that, 28.0 mL solution in total was transferred into a 40.0 mL stainless steel Teflon-lined autoclave. Then, the cleanly ITO substrate was introduced into the precursor solution. The autoclave was kept in a bake oven at 210 °C for 24 h. Finally, the ITO substrate was purged in deionized water for several times and dried in air for further characterization.

Characterization

The structural characterization of the SnO_2 NFRAs was done on ITO substrate at incidence angle of 2.0° by using X-ray diffraction (XRD, 6100, SHIMADZU) equipped with Cu Kα X-ray source operated at 40 kV and 30 mA. The scan rate of 6°/min and step size of 0.02° were used. The products were imaged using scanning electron microscope (SEM, Zeiss ΣIGMA/VP) at 3 kV with a working distance of ~9 mm. Energy dispersive spectroscopy (EDS) was carried out at 15 kV under the SEM. Transmission electron microscope (TEM) studies were performed on JEM-3010 at operating voltage of 200 keV. The PL spectrum was recorded with a FluoroMax-4 spectrophotometer (Horiba Jobin-Yvon) with a Xe lamp and a 360 nm filter was used. Quantum yield was acquired on the same FluoroMax-4 spectrophotometer equipping with the integrating sphere. The Raman spectrum was acquired by using a Renishaw inVia micro-Raman spectrometer at room temperature, and a laser with 514.5 nm wavelength was used as the excitation light source. The ultraviolet–visible (UV–Vis) diffuse reflectance spectrum (DRS) is recorded with a UV–Vis-NIR spectrophotometer (Cary 4000, VARIAN, USA).

Results and discussion

The crystalline structure of the obtained product was checked by XRD as shown in Fig. 1. The diffraction peaks are in accordance with rutile of SnO_2 (space group $P42/mnm$ (136), JCPDS file No. 41-1445). The result shows that the pure SnO_2 sample has been synthesized successfully.

When ITO substrate was introduced into the precursor solution, SnO_2 nanorod arrays could be readily grown on the substrate, decorated or covered by a layer of hierarchical SnO_2 nanoflowers. As shown in Fig. 2, SnO_2 nanoflowers are spread onto the SnO_2

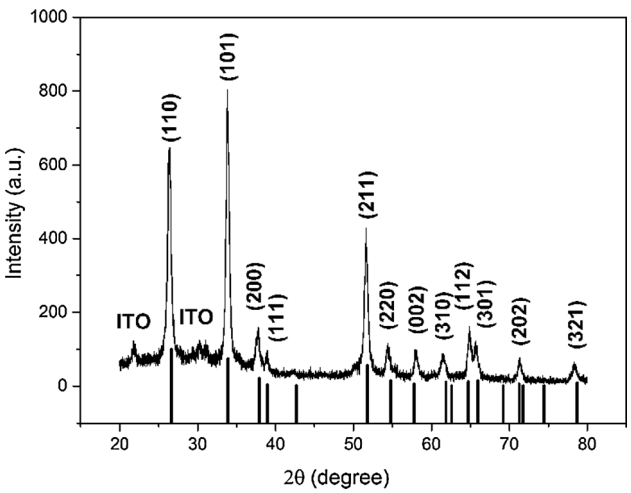

Figure 1 XRD pattern of the SnO_2 NFRAs.

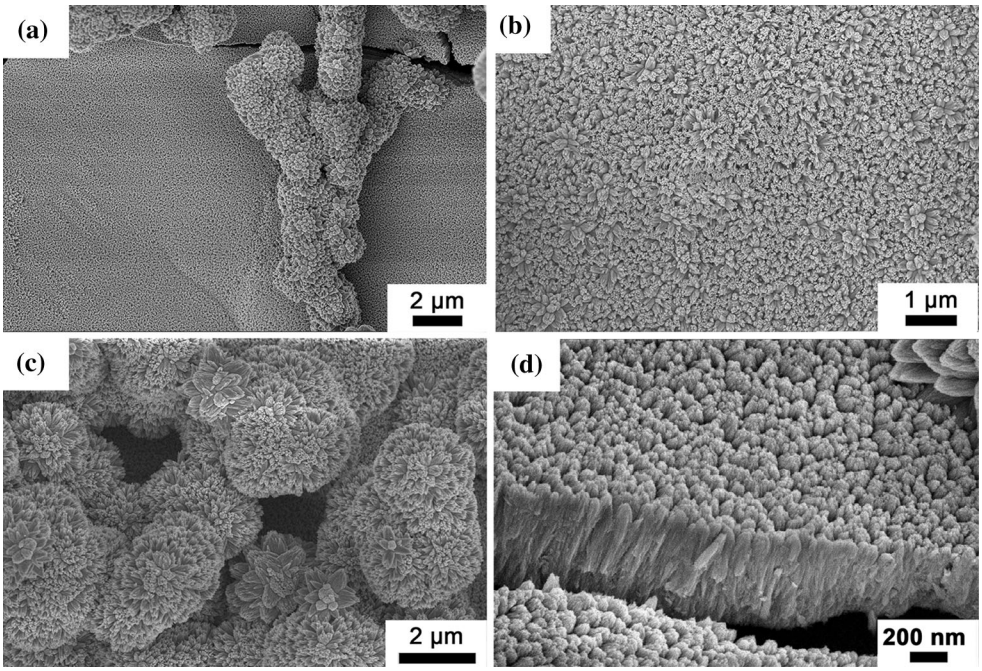

Figure 2 Top and cross section views of SEM images of the hierarchical SnO_2 NFRAs architecture on ITO substrate, top views (**a**–**c**) and cross section view (**d**).

nanorod arrays and the nanoflowers and nanorod arrays can be observed synchronously in Fig. 2a. Figure 2b, d shows the top views and the cross section view of the SnO_2 nanorod arrays with a diameter of 100 nm and length of 600 nm, which indicates that the SnO_2 grown on the ITO substrate uniformly and compactly. In Fig. 2c, there are many nanoflowers, but the nanorod arrays are sightless, because the nanoflowers are plentiful and covered nanorod arrays. The TEM images of the hierarchical SnO_2 NFRAs architecture are shown in Fig. 3. For measuring TEM, SnO_2 NFRAs are scraped from the ITO substrate. The nanorod arrays are peeled off from the ITO substrate as shown in Fig. 3a, b. It is necessary to emphasize the fact that the SnO_2 nanorod arrays epitaxially grow on the ITO substrate via the hydrothermal process. The HRTEM image from a single nanorod in Fig. 3c shows that the lattice spacing is 0.326 nm, which is corresponding to the interspacing of the (110) planes, indicating that the [001] direction is the preferential growth direction of SnO_2. The fast Fourier transform (FFT) pattern in Fig. 3c (inset) also confirms the estimation that the growth was along the c axis, which was same with our previous report growth mode [27].

In order to analyze the stoichiometric proportion of the comprised elements in as-prepared product, the EDS measurement has been carried out under the SEM. Figure 4 shows the EDS spectra of SnO_2 nanorod arrays (Fig. 4a) and SnO_2 nanoflowers (Fig. 4b). The values of the atomic ratio between O and Sn are 61.88:38.12 and 49.28:50.72 in SnO_2 nanorod arrays and SnO_2 nanoflowers, respectively, which means that there are some oxygen vacancy (V_O) defects existing in both nanorod arrays and nanorod flowers architectures. The observed atomic ratio of Sn and O verifies the formation of nonstoichiometric phase of tin oxide. Therefore, the SnO_2 NFRAs were annealed in the oxygen environment at 800 °C for 4 h. The EDS spectra of SnO_2 nanorod arrays and SnO_2 nanoflowers are shown in Fig. S1a and Fig. S1b, respectively, and corresponding atomic ratio between O and Sn is 69.16:30.84 and 67.25:32.75, which means the stoichiometric phase of tin oxide can be obtained.

Based on the above characterizations, a reasonable growth mechanism of the SnO_2 NFRAs structures can be proposed. The major reaction equations during the reaction processes can be summarized as follows: [23, 28]

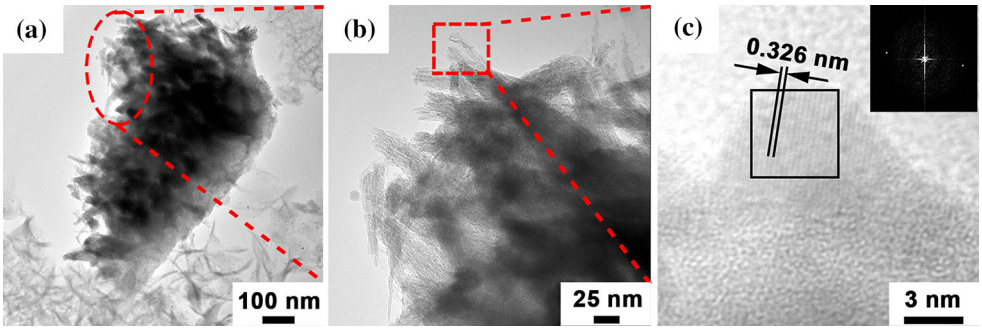

Figure 3 TEM images of SnO_2 nanorod arrays (**a**, **b**), HRTEM image (**c**) of SnO_2 nanorod with corresponding fast Fourier transform (FFT) image (*inset*) taken from the *black square*.

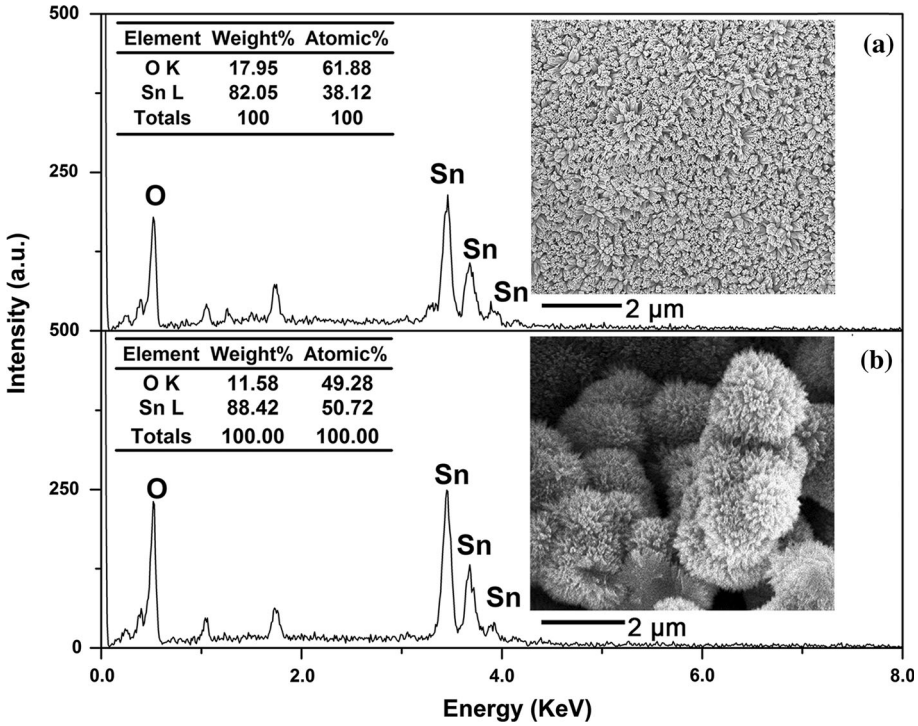

Figure 4 EDS spectra of SnO_2 nanorod arrays (**a**) and SnO_2 nanoflowers (**b**).

$$Sn^{4+} + 4OH^- \rightarrow Sn(OH)_4 \quad (1)$$

$$Sn(OH)_4 + 2OH^- \rightarrow Sn(OH)_6^{2-} \rightarrow SnO_2. \quad (2)$$

At the initial stage, while the NaOH solution was added into $SnCl_4$ solution drop by drop, amounts of white precipitates $Sn(OH)_4$ were produced (Eq. 1). Along with the drop process, the $Sn(OH)_4$ was dissolved by the excess OH^- to generate $Sn(OH)_6^{2-}$ complex ions (Eq. 2), which was the basic cells of crystalline growth. There were large numbers of SnO_2 seeds lying on the surface of the ITO substrate randomly, which offered an active sites of the SnO_2 nanorod. Synthesizing SnO_2 flowers usually required the formation of aggregated SnO_2 nuclei in an initial homogeneous nucleation process. In the basic environment at room temperature, only a few basic cells could be hydrolyzed into SnO_2 nanocrystals. However, during the hydrothermal condition, SnO_2 basic cells hydrolyzation into nanocrystals could be accelerated, and then the SnO_2 nanocrystals could be aggregated into SnO_2 and oriented growth with the driving force of decreasing surface energy. In the reaction system, the nanorod arrays were grown on the ITO substrate and the nanoflowers formed in the solution at the same time. Following this, low formation energy of the heterogeneous crystal growth made few SnO_2 nanocrystalline grow on the ITO substrate. Then, the ITO substrate served as seed

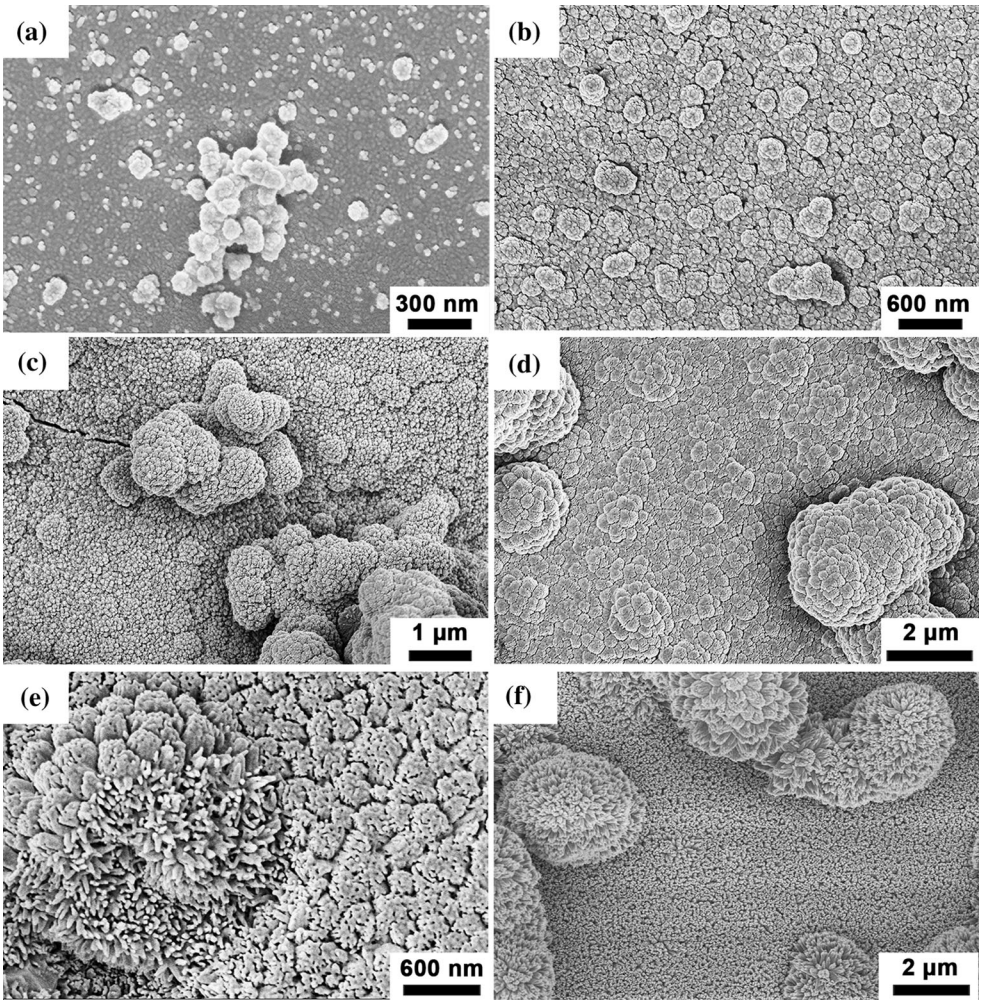

Figure 5 SEM images of hierarchical SnO_2 NFRAs after different hydrothermal reaction times: **a** 15 min, **b** 30 min, **c** 2 h, **d** 8 h, **e** 16 h, **f** 24 h.

layer and guided the nucleation of SnO_2, which promoted the SnO_2 nucleation and grown into nanorod arrays in the hydrothermal progress. Moreover, without the inducing effect of the ITO layer, SnO_2 nanorod would also be produced in solution and tend to aggregate into a spherical morphology because the spherical materials reunited for high stability and low surface energy. The SnO_2 nanoflowers deposited on the top of SnO_2 nanorod arrays via natural precipitation [19].

For investigating the growth mechanism of the hierarchical SnO_2 NFRAs, a series of experiments were carried out along with the reaction time, and corresponding SEM images of the hierarchical SnO_2 NFRAs are shown in Fig. 5. Based on the morphology evolution process, the schematic illustration of the morphology evolution process can be established (Fig. 6). When the ITO was immersed in the precursor solution, the SnO_2 growth units were formed in the precursor solution and grown on the substrate at the same time due to its heterogeneous nucleation. When the reaction time reaches at 15 min, the SnO_2 growth units can flock together based on the seeds layer in the ITO and these nuclei also reunite to form the multitwin central nuclei under the synergistic interaction from Van der Waals force (Figs. 5a, 6a) [27]. The SnO_2 nuclei further increasingly constitute the SnO_2 grain with a diameter about 200 nm, and some perching sites protrude on the surface of the SnO_2 grain in this stage (Figs. 5b, 6b). Following these perching sites, the bud can grow on the surface of the grain, which is made up of dozens of nanorod (Figs. 5c, 6c). Similarly, the bud is growing on the grain which is located at the ITO (Figs. 5c, 6c). The

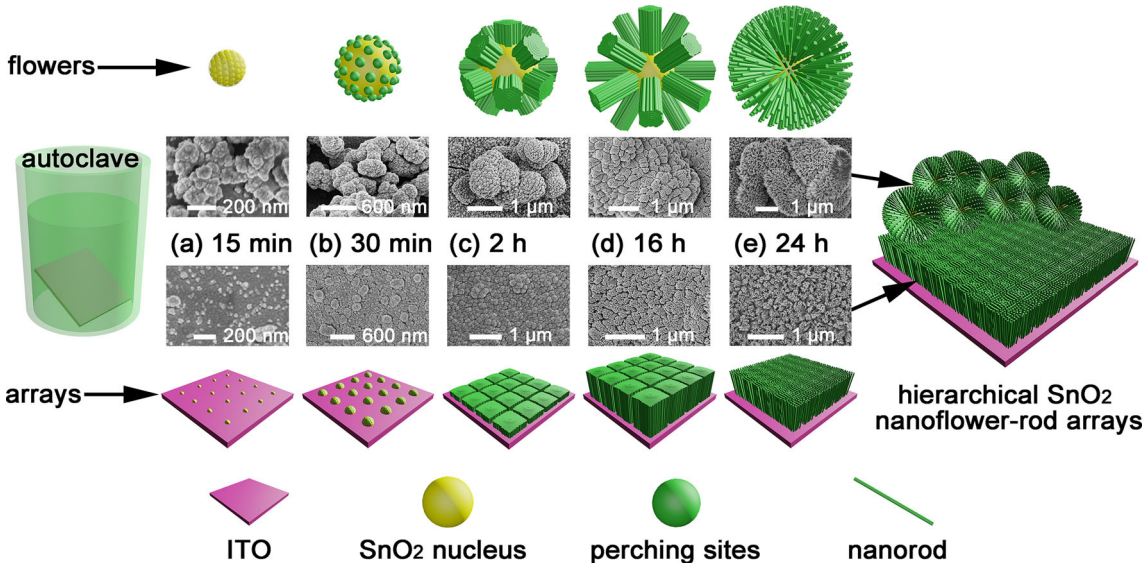

Figure 6 Schematic illustration of the reasonable evolution processes of hierarchical SnO_2 NFRAs.

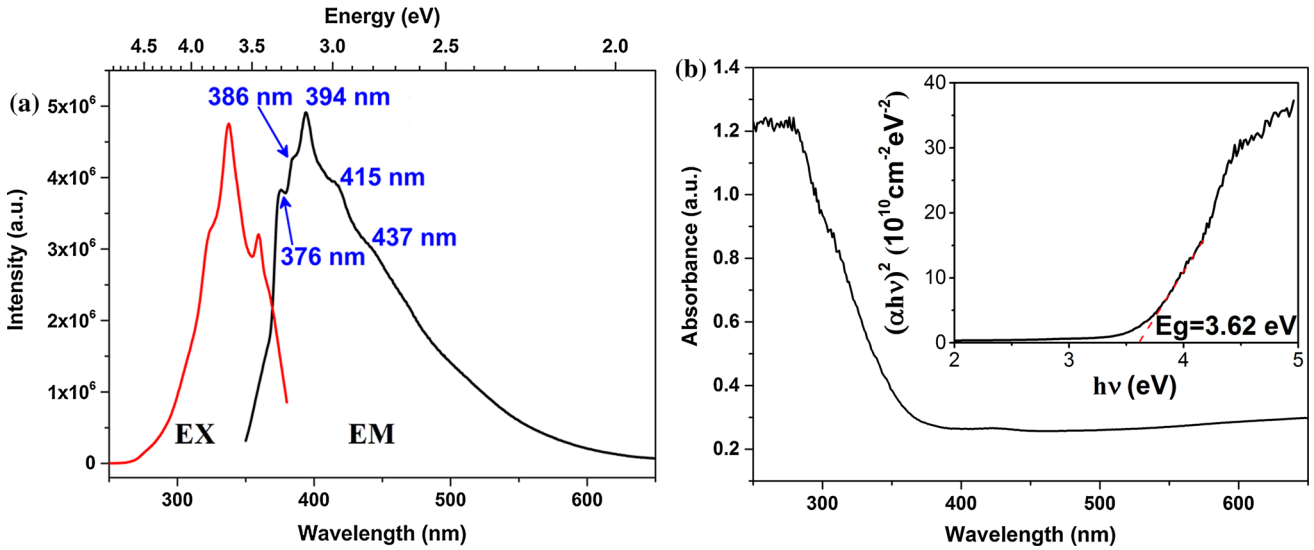

Figure 7 The emission spectrum of hierarchical SnO_2 NFRAs under 337 nm excitation of Xe lamp and corresponding excitation spectrum at emission energy of 394 nm (**a**). The UV–Vis absorbance spectrum of hierarchical SnO_2 NFRAs (**b**).

growth rate of the bud is attenuate while its length is on the verge of 600 nm (Figs. 5d, 6d), and some of the buds begin to bloom (Figs. 5e, 6d). As the reaction time goes on, the bud is in full bloom. The nanoflower and the nanorod arrays can be constructed at 24 h (Figs. 5f, 6e); the flowers deposit on the ITO substrate, and the complex hierarchical SnO_2 nanoflower-rod arrays can be obtained. Cross section views of hierarchical SnO_2 nanomaterials and ITO substrate in above reaction intervals are shown in Fig. S1, indicating a consistent evolution process. The microstructural information of the SnO_2 homogeneous nucleation on ITO substrate directing SnO_2 further growth into nanorod by increasing the hydrothermal reaction time. Therefore, the ITO is believed to serve as a seed layer at the stage of homogeneous nucleation.

The excitation and emission spectra of hierarchical SnO_2 NFRAs are shown in Fig. 7a. The excitation spectrum is recorded at emission energy of 394 nm.

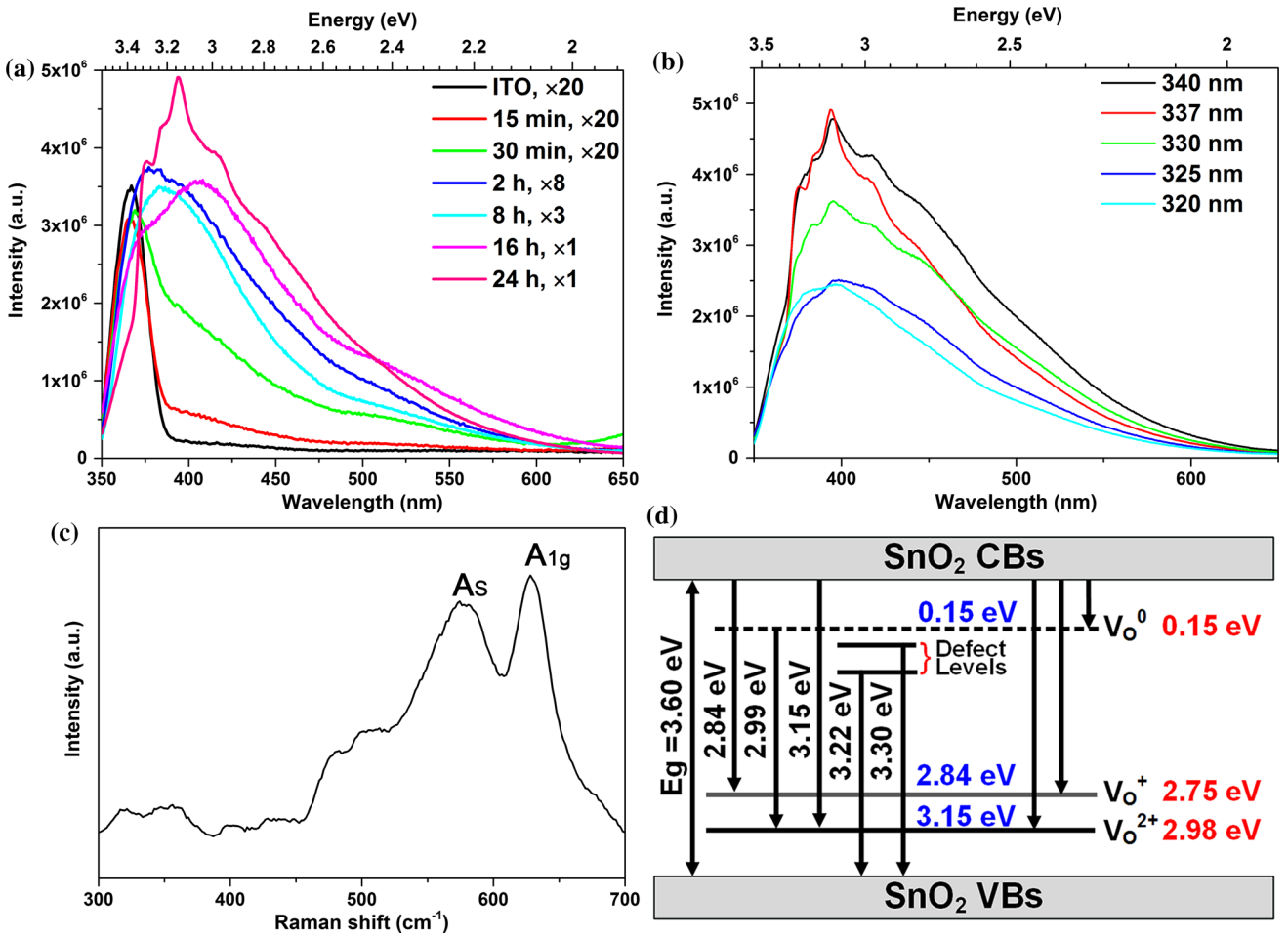

Figure 8 Reaction time-dependent PL spectra of SnO_2 nanomaterials (**a**). The excitation wavelength-dependent emission spectra of hierarchical SnO_2 NFRAs (**b**). Raman spectra of the SnO_2 NFRAs (**c**). The diagram of relaxation process in photoexcited SnO_2 (**d**, *left*) and the energy levels comparison of the V_O with different charge states in band gap (**d**, *right*, the PL analysis results (*blue*) and the DFT calculated results (*red*).

The emission spectrum is recorded with the excitation wavelength of 337 nm in the spectral range of 350–650 nm, which is composed of an intensive UV-violet peak at 394 nm, and four shoulders at 376, 386, 415, and 437 nm (the quantum yield is 2.62 %). The sharp features of the emission spectrum should be caused by the sharp features of the excitation spectrum. Figure 7b exhibits the UV–Vis absorbance spectrum of hierarchical SnO_2 NFRAs; the inset of $(\alpha hv)^2$ vs hv can be derived from the absorption data. As shown in Fig. 7b, the average band gap value of the SnO_2 NFRAs is ~3.62 eV, which is slightly larger than that of bulk materials. In order to investigate the impact of hierarchical morphology on the PL property. The reaction time-dependent PL spectra of SnO_2 nanomaterials are shown in Fig. 8a with an excitation wavelength of 337 nm. There is a weak emission peak of the ITO substrate centered at 368 nm. With the increase of reaction time, the intensity of the defect-related emission increases. When the reaction time reaches at 2 h, the SnO_2 nanomaterials cover the ITO substrate completely (Fig. 5c), which results in the disappearance of the emission peak of ITO substrate. The intensity of the defect-related emission further increased until the hierarchical SnO_2 NFRAs formed. The bud of SnO_2 is in full bloom with the reaction time goes on (Fig. 5e), which enlarges the surface of SnO_2 and results in the defect-related emission. The excitation wavelength-dependent emission spectra of hierarchical SnO_2 NFRAs are shown in Fig. 8b. Interestingly, the position of emission peaks almost does not vary with the increasing of excitation wavelength; the intensity increases gradually as excitation spectrum increases from 320 to 340 nm,

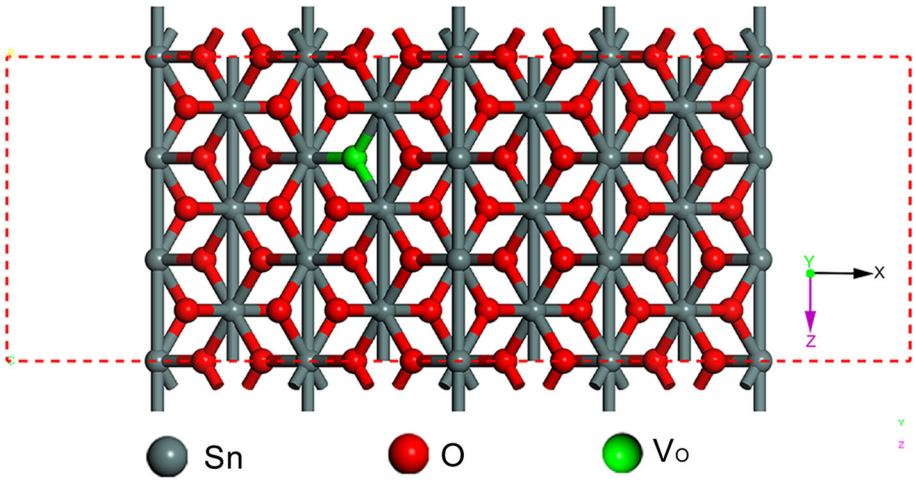

Figure 9 Schematic illustration of SnO_2 nanowire model (*gray*, *red*, *green color* represent tin atom, oxygen atom, oxygen vacancy).

and the similar phenomenon of SnO_2 nanomaterials has been reported [29, 30]. The Raman spectrum of the SnO_2 NFRAs is displayed in the inset of Fig. 8c. The Raman peak locating at 628 cm^{-1} corresponding to the A_{1g} modes, which is in good agreement with for the rutile bulk SnO_2 [30, 31]. The Raman peak locating at 574 cm^{-1} corresponding to the A_S modes, which indicated that there are V_O in the SnO_2 materials [30, 32].

Generally, V_O are known as the most common defects in SnO_2, which usually play a role in radiative centers in luminescence processes on SnO_2 grain boundaries and arouse to defect level emission [33–39]. In the previous discussions, the EDS and Raman results indicate that the V_O defects are existed in the NFRAs. Therefore, we could conclude that V_O are the main origin of the luminescence in comparison with the EDS and Raman results. The V_O are the intrinsic defects in n-type SnO_2, which can capture electrons and form ionized vacancies [38, 39]. There are three types of V_O in SnO_2 with different charge states namely V_O^0, V_O^+, and V_O^{2+} [34–37, 40]. The ionized vacancies in SnO_2 can play a role as deep defect donors and form new energy levels, which further influences the PL properties of SnO_2 [41, 42]. In fact, the V_O^0 state is a shallow donor near the conduction bands (CBs). Most of the V_O state are V_O^+ state, which are located under flat-band conditions. Furthermore, V_O^{2+} state is V_O^+ state combining with a hole. When the bands gap of SnO_2 is smaller than the energy of the excitation photon, the electron can be excited to the CBs. Then, the V_O^+ state receives a hole from the valence bands (VBs) and hence the V_O^{2+} is created. Undeniably, the intensity of V_O^{2+} states will increase. Accordingly, the photoexcited electrons can recombine with V_O^+ or V_O^{2+} state. More specifically, the peak near 437 nm (~2.84 eV), is attributed to V_O^+ in the SnO_2 nanorod arrays [33–35], i.e., the radiative transition of the V_O^+ level to the CBs of SnO_2. The 415 nm (~2.99 eV) peak can be explained by the V_O^0 [40], which is caused by the combination of the electron from V_O^0 level and a hole donated by V_O^{2+} level. The 394 nm (~3.15 eV) emission peak is attributed to the combination of the electron from CBs and a hole from the V_O^{2+} [35]. The 386 nm (~3.22 eV) emission peak only can be observed in our case, and it might attribute to the relaxation process of defects level to VBs. The 376 nm (~3.30 eV) emission peak is related to the impurity or defect concentration and not to the structure [43]. The energy levels of V_O^0 state, V_O^+ state, V_O^{2+} state center at 0.15, 2.84, and 3.15 eV in band gap, respectively.

It is known that different defects may cause different energy levels, which will be reflected on the spectrum (such as PL spectrum), and the spectrum can be measured directly in experiments [44–47]. The PL spectrum generally reflects the relaxation process in photoexcited materials. Furthermore, based on the first principles study, the mechanism of the PL spectrum can be explained more credibly. Additionally, the explanations of the luminous mechanism are accordant both in real materials and in first principles study [44, 45, 48–50]. Even so, there are few reports about the luminous mechanism in SnO_2 based on the first principles study. Therefore, in order to further confirm the PL results, the exact energy level of V_O,

V_O^+, and V_O^{2+} in SnO_2 should be confirmed. Along this line of consideration, a DFT study is proceeded with the pristine and the defective SnO_2 nanowire models. The schematic illustration of SnO_2 nanowire model containing 75 atoms with a vacuum region up to 9.475 Å is shown in Fig. 9. All the calculations are computed by using the CASTEP software package in Materials Studios 5.0. The exchange correlation potential is described with the local-density approximation (LDA). The cutoff energy of plane wave is set as 400 eV. The Brillouin zone integration is approximated using k-point sampling scheme of Monkhorst–Pack and 1 × 1 × 8 k-point grids are used. The tolerance for self-consistent filed, energy, maximum force, maximum displacement, and maximum stress are set as 1.0×10^{-6} eV/atom, 1.0×10^{-5} eV/atom, 0.03 eV/Å, 1.0×10^{-3} Å, and 0.05 GPa, respectively.

In order to understand the relationship between defects structure and PL properties in SnO_2 NFRAs, the ionization energy of V_O with different types of charge states in SnO_2 is calculated. The formation energy of an isolated neutral V_O in SnO_2 is defined by the equation as follows: [48, 51, 52]

$$E^f\left[V_O^q\right] = E_{tot}\left[V_O^q\right] - E_{tot}[\text{pristine}] - \sum n_x \cdot \mu_x + q\left(E_f + E_v + \Delta V\right), \quad (3)$$

where $E_{tot}[V_O^q]$ is the total energy of the nanowire model containing one oxygen vacancy with q charge. E_{tot}[pristine] is the total energy of the prefect nanowire model. The n_x is the number of the defect atom and the μ_x is chemical potential of the defect atom. The E_f, E_v, and ΔV are, respectively, refer to the Fermi level, the formation energy of the charged state, and the correction term. The ionization energy namely E_A is computed by the following equation: [48]

$$E^f\left[V_O^*\right](E_F = E_A) = E^f\left[V_O^0\right]. \quad (4)$$

In the case of V_O, the formation energy of the V_O^0 state centers at about 0.15 eV, and the ionization energy of the V_O^+ state and V_O^{2+} state center at about 2.75 and 2.98 eV, respectively. Compared with the energy level deduced in PL spectrum, the V_O^0 state, V_O^+ state, and V_O^{2+} state in band gap are 0.15, 2.84, and 3.15 eV respectively. The energy level diagram is shown in Fig. 8d and all the energy levels are respected to the VBs of prefect SnO_2. The V_O^0 state is centered at about 0.15 eV both in real SnO_2 NFRAs and the computation results, and the result is consistent with previous reports [53–55]. Furthermore, the computation results of the V_O^+ and V_O^{2+} states are centered all close to the real SnO_2 NFRAs product. Inevitably, there are still have few deviations about 0.09 eV (V_O^+) and 0.17 eV (V_O^{2+}), which is caused by the concentration of V_O in the nanowires module. The concentration of V_O is directly related to the total atoms in SnO_2 nanowires module. More specifically, on the one hand, the small SnO_2 nanowire model results in the high concentration of V_O. The calculations with the 75 atoms nanowires model show that the ionization energy is converged well for this system size, indicating that there is a significant defect–defect interaction. On the other hand, the computational efficiency is directly affected by the system size of the SnO_2 nanowire model. Consequently, a SnO_2 nanowire model containing 75 atoms is chosen to confirm the PL results. Videlicet, the calculation of the V_O in SnO_2 can confirm the luminous mechanism in this report.

Conclusions

The SnO_2 NFRAs are synthesized on the ITO substances through a template-free hydrothermal method. A reasonable growth mechanism of the SnO_2 NFRAs architecture has been proposed. The ITO substrate plays a role of seed layer and guides the nucleation of SnO_2 NFRAs. The PL property of SnO_2 has been analyzed based on the PL spectrum, which are composed of an intensive UV-violet peak at 394 nm, and four shoulders at 376, 386, 415, and 437 nm. The three types of V_O are regarded as luminescence mechanism, and the V_O^0 state, V_O^+ state, and V_O^{2+} state in band gap are 0.15, 2.84, and 3.15 eV, respectively. The SnO_2 nanowire model containing 75 atoms is chosen to confirm the PL results. The DFT calculation discloses that the ionization energy of the V_O^+ state and V_O^{2+} state center at about 2.75 and 2.98 eV, respectively, which is in agreement with the PL spectrum.

Acknowledgements

This work was supported by the National Natural Science Foundation of China (Grants 61306009 and 61405159), the Key Project of Natural Science Foundation of Shaanxi Province (Grants 2014JZ2-003), the Natural Science Foundation of Shaanxi Province

(Grants 2014JM8339 and 2015JM6274), the Science and Technology Star Project of Shaanxi Province (Grants 2013KJXX-24), and the NWU Graduate Innovation and Creativity Funds (YZZ15010).

Compliance with ethical standards

Conflict of interest The authors declare that they have no competing financial interest.

Electronic supplementary material: The online version of this article (doi:10.1007/s10853-016-0169-0) contains supplementary material, which is available to authorized users.

References

[1] Lupan O, Chow L, Chai G, Heinrich H, Park S, Schulte A (2009) Synthesis of one-dimensional SnO_2 nanorods via a hydrothermal technique. Physica E 41(4):533–536. doi:10.1016/j.physe.2008.10.001

[2] Sun P, Mei XD, Cai YX, Ma J, Sun YF, Liang XS, Liu FM, Lu GY (2013) Synthesis and gas sensing properties of hierarchical SnO_2 nanostructures. Sensor Actuat B-Chem 187:301–307. doi:10.1016/j.snb.2012.11.043

[3] Chen Z, Tian YF, Li SJ, Zheng HW, Zhang WF (2012) Electrodeposition of arborous structure nanocrystalline SnO_2 and application in flexible dye-sensitized solar cells. J Alloys Compd 515:57–62. doi:10.1016/j.jallcom.2011.10.116

[4] Duong TT, Choi HJ, He QJ, Le AT, Yoon SG (2013) Enhancing the efficiency of dye sensitized solar cells with an SnO_2 blocking layer grown by nanocluster deposition. J Alloys Compd 561:206–210. doi:10.1016/j.jallcom.2013.01.188

[5] Zhang DF, Sun LD, Xu G, Yan CH (2006) Size-controllable one-dimensinal SnO_2 nanocrystals: synthesis, growth mechanism, and gas sensing property. PCCP 8(42):4874–4880. doi:10.1039/B604560J

[6] Wang H, Liang QQ, Wang WJ, An YR, Li JH, Guo L (2011) Preparation of flower-like SnO_2 nanostructures and their applications in gas-sensing and lithium storage. Cryst Growth Des 11(7):2942–2947. doi:10.1021/cg2001255

[7] Wang X, Liu W, Yang H, Li X, Li N, Shi R, Zhao H, Yu J (2011) Low-temperature vapor–solid growth and excellent field emission performance of highly oriented SnO_2 nanorod arrays. Acta Mater 59(3):1291–1299. doi:10.1016/j.actamat.2010.10.061

[8] Shao F, Hoffmann MWG, Prades JD, Zamani R, Arbiol J, Morante JR, Varechkina E, Rumyantseva M, Gaskov A, Giebelhaus I, Fischer T, Mathur S, Hernández-Ramírez F (2013) Heterostructured p-CuO (nanoparticle)/n-SnO_2 (nanowire) devices for selective H_2S detection. Sens Actuator B-Chem 181:130–135. doi:10.1016/j.snb.2013.01.067

[9] Mutinati GC, Brunet E, Koeck A, Steinhauer S, Yurchenko O, Laubender E, Urban G, Siegert J, Rohracher K, Schrank F, Schrems M (2014) Optimization of CMOS integrated nanocrystalline SnO_2 gas sensor devices with bimetallic nanoparticles. Proc Eng 87:787–790. doi:10.1016/j.proeng.2014.11.679

[10] Huh J, Na J, Ha JS, Kim S, Kim GT (2011) Asymmetric contacts on a single SnO_2 nanowire device: an investigation using an equivalent circuit model. ACS Appl Mater Inter 3(8):3097–3102. doi:10.1021/am2006096

[11] Wang XL, Aroonyadet N, Zhang YZ, Mecklenburg M, Fang X, Chen H, Goo E, Zhou CW (2014) Aligned epitaxial SnO_2 nanowires on sapphire: growth and device applications. Nano Lett 14(6):3014–3022. doi:10.1021/nl404289z

[12] Liu Y, Koep E, Liu ML (2005) A highly sensitive and fast-responding SnO_2 sensor fabricated by combustion chemical vapor deposition. Chem Mater 17(15):3997–4000. doi:10.1021/cm050451o

[13] Kida T, Doi T, Shimanoe K (2010) Synthesis of monodispersed SnO2 nanocrystals and their remarkably high sensitivity to volatile organic compounds. Chem Mater 22(8):2662–2667. doi:10.1021/cm100228d

[14] D'Arienzo M, Cristofori D, Scotti R, Morazzoni F (2013) New Insights into the SnO_2 sensing mechanism based on the properties of shape controlled tin oxide nanoparticles. Chem Mater 25(18):3675–3686. doi:10.1021/cm401895x

[15] Deng KM, Lu H, Shi ZW, Liu Q, Li L (2013) Flexible three-dimensional SnO_2 nanowire arrays: atomic layer deposition-assisted synthesis, excellent photodetectors, and field emitters. ACS Appl Mater Inter 5(16):7845–7851. doi:10.1021/am401762y

[16] Rakshit T, Santra S, Manna I, Ray SK (2014) Enhanced sensitivity and selectivity of brush-like SnO2 nanowire/ZnO nanorod heterostructure based sensors for volatile organic compounds. RSC Adv 4(69):36749–36756. doi:10.1039/C4RA05914J

[17] Xu L, Xing R, Song J, Xu W, Song H (2013) ZnO-SnO_2 nanotubes surface engineered by Ag nanoparticles: synthesis, characterization, and highly enhanced HCHO gas sensing properties. J Mater Chem C 1(11):2174–2182. doi:10.1039/C3TC00689A

[18] Zhao XY, Liu B, Hu CW, Cao MH (2014) In situ growth of hierarchical SnO_2 nanosheet arrays on 3D macroporous substrates as high-performance electrodes. Chem Eur J 20(2):467–473. doi:10.1002/chem.201303548

[19] Wang HK, Kalytchuk S, Yang HH, He LF, Hu CY, Teoh WY, Rogach AL (2014) Hierarchical growth of SnO_2

nanostructured films on FTO substrates: structural defects induced by Sn(ii) self-doping and their effects on optical and photoelectrochemical properties. Nanoscale 6(11):6084–6091. doi:10.1039/C4NR00672K

[20] Niu HH, Zhang SW, Wang RB, Guo ZQ, Shang X, Gan W, Qin SX, Wan L, Xu JZ (2014) Dye-sensitized solar cells employing a multifunctionalized hierarchical SnO_2 nanoflower structure passivated by TiO_2 nanogranulum. J Phys Chem C 118(7):3504–3513. doi:10.1021/jp409203w

[21] Zhang HL, Hu CG (2011) Effective solar absorption and radial microchannels of SnO_2 hierarchical structure for high photocatalytic activity. Catal Commun 14(1):32–36. doi:10.1016/j.catcom.2011.07.012

[22] Fu MS, Ni L, Du N (2014) Self-templated porous hierarchical SnO_2 ceramics with enhanced lithium storage capacity. J Alloys Compd 591:65–71. doi:10.1016/j.jallcom.2013.12.177

[23] Wang SR, Yang JD, Zhang HX, Wang YS, Gao XL, Wang LW, Zhu ZY (2015) One-pot synthesis of 3D hierarchical SnO_2 nanostructures and their application for gas sensor. Sens Actuator B-Chem 207:83–89. doi:10.1016/j.snb.2014.10.032

[24] Yin JZ, Wang XF, Li RQ, Wang GC, Zhang WG (2013) Synthesis and characterization of hierarchical SnO_2 hollow octahedra. Mater Lett 113:118–121. doi:10.1016/j.matlet.2013.09.058

[25] Wang YN, Dai QQ, Yang XY, Zou B, Li DM, Liu BB, Hu MZ, Zou GT (2011) A facile approach to PbS nanoflowers and their shape-tunable single crystal hollow nanostructures: morphology evolution. CrystEngComm 13(1):199–203. doi:10.1039/C004459H

[26] Wang HK, Rogach AL (2014) Hierarchical SnO_2 nanostructures: recent advances in design, synthesis, and applications. Chem Mater 26(1):123–133. doi:10.1021/cm4018248

[27] Tian JX, Zhang ZY, Yan JF, Ruan XF, Yun JN, Zhao W, Zhai CX (2014) Hydrothermal synthesis and infrared emissivity property of flower-like SnO_2 particles. AIP Adv 4(4):047131. doi:10.1063/1.4873536

[28] Jiang XH, Ma SY, Sun AM, Xu XL, Li WQ, Wang TT, Jin WX, Luo J, Cheng L, Mao YZ (2015) 3D porous flower-like SnO_2 microstructure and its gas sensing properties for ethanol. Mater Lett 159:5–8. doi:10.1016/j.matlet.2015.06.050

[29] Zhou GX, Xiong SJ, Wu XL, Liu LZ, Li TH, Chu PK (2013) N-doped SnO_2 nanocrystals with green emission dependent upon mutual effects of nitrogen dopant and oxygen vacancy. Acta Mater 61(19):7342–7347. doi:10.1016/j.actamat.2013.08.040

[30] Liu LZ, Wu XL, Xu JQ, Li TH, Shen JC, Chu PK (2012) Oxygen-vacancy and depth-dependent violet double-peak photoluminescence from ultrathin cuboid SnO_2 nanocrystals. Appl Phys Lett 100(12):121903. doi:10.1063/1.3696044

[31] Kar A, Kundu S, Patra A (2011) Surface defect-related luminescence properties of SnO_2 nanorods and nanoparticles. J Phys Chem C 115(1):118–124. doi:10.1021/jp110313b

[32] Liu LZ, Wu XL, Gao F, Shen JC, Li TH, Chu PK (2011) Determination of surface oxygen vacancy position in SnO_2 nanocrystals by Raman spectroscopy. Solid State Commun 151(11):811–814. doi:10.1016/j.ssc.2011.03.029

[33] Zhou JX, Zhang MS, Hong JM, Yin Z (2006) Raman spectroscopic and photoluminescence study of single-crystalline SnO_2 nanowires. Solid State Commun 138(5):242–246. doi:10.1016/j.ssc.2006.03.007

[34] Gu F, Wang SF, Song CF, Lü MK, Qi YX, Zhou GJ, Xu D, Yuan DR (2003) Synthesis and luminescence properties of SnO_2 nanoparticles. Chem Phys Lett 372(3–4):451–454. doi:10.1016/S0009-2614(03)00440-8

[35] Gu F, Wang SF, Lü MK, Cheng XF, Liu SW, Zhou GJ, Xu D, Yuan DR (2004) Luminescence of SnO_2 thin films prepared by spin-coating method. J Cryst Growth 262(1–4):182–185. doi:10.1016/j.jcrysgro.2003.10.028

[36] Hu JQ, Bando Y, Golberg D (2003) Self-catalyst growth and optical properties of novel SnO_2 fishbone-like nanoribbons. Chem Phys Lett 372(5–6):758–762. doi:10.1016/S0009-2614(03)00503-7

[37] Kılıç Ç, Zunger A (2002) Origins of coexistence of conductivity and transparency in SnO_2. Phys Rev Lett 88(9):095501. doi:10.1103/PhysRevLett.88.095501

[38] Du Y, Zhang MS, Hong J, Shen Y, Chen Q, Yin Z (2003) Structural and optical properties of nanophase zinc oxide. Appl Phys A 76(2):171–176. doi:10.1007/s003390201404

[39] Gao T, Wang TH (2008) Vapor phase growth and optical properties of single-crystalline SnO_2 nanobelts. Mater Res Bull 43(4):836–842. doi:10.1016/j.materresbull.2007.05.004

[40] Wang B, Yang YH, Wang CX, Yang GW (2005) Growth and photoluminescence of SnO_2 nanostructures synthesized by Au–Ag alloying catalyst assisted carbothermal evaporation. Chem Phys Lett 407(4–6):347–353. doi:10.1016/j.cplett.2005.03.119

[41] Li PG, Guo X, Wang XF, Tang WH (2009) Synthesis, photoluminescence and dielectric properties of O-deficient SnO_2 nanowires. J Alloys Compd 479(1–2):74–77. doi:10.1016/j.jallcom.2009.01.054

[42] Gu F, Wang SF, Lü MK, Zhou GJ, Xu D, Yuan DR (2004) Photoluminescence properties of SnO_2 nanoparticles synthesized by sol–gel method. J Phys Chem B 108(24):8119–8123. doi:10.1021/jp036741e

[43] Jeong J, Choi SP, Chang CI, Shin DC, Park JS, Lee BT, Park YJ, Song HJ (2003) Photoluminescence properties of SnO_2

thin films grown by thermal CVD. Solid State Commun 127(9–10):595–597. doi:10.1016/S0038-1098(03)00614-8

[44] Hu J, Pan BC (2009) The optical and vibrational properties of dominant defects in undoped ZnO: a first-principles study. J Appl Phys 105(8):083710. doi:10.1063/1.3109207

[45] Liu LZ, Xu JQ, Wu XL, Li TH, Shen JC, Chu PK (2013) Optical identification of oxygen vacancy types in SnO_2 nanocrystals. Appl Phys Lett 102(3):031916. doi:10.1063/1.4789538

[46] Long D (1962) Energy bands in semiconductors. J Appl Phys 33(5):1682–1696. doi:10.1063/1.1728811

[47] Roman LS, Valaski R, Canestraro CD, Magalhães ECS, Persson C, Ahuja R, da Silva Jr EF, Pepe I, da Silva AF (2006) Optical band-edge absorption of oxide compound SnO_2. Appl Surf Sci 252(15):5361–5364. doi:10.1016/j.apsusc.2005.12.040

[48] Van de Walle CG, Neugebauer J (2004) First-principles calculations for defects and impurities: applications to III-nitrides. J Appl Phys 95(8):3851–3879. doi:10.1063/1.1682673

[49] Li HL, Lv YB, Li JZ, Yu K (2014) Experimental and first-principles studies of structural and optical properties of rare earth (RE = La, Er, Nd) doped ZnO. J Alloys Compd 617:102–107. doi:10.1016/j.jallcom.2014.08.019

[50] Paul S, Chetri P, Choudhury A (2014) Effect of manganese doping on the optical property and photocatalytic activity of nanocrystalline titania: experimental and theoretical investigation. J Alloys Compd 583:578–586. doi:10.1016/j.jallcom.2013.08.209

[51] Li JB, Wei SH, Li SS, Xia JB (2006) Design of shallow acceptors in ZnO: first-principles band-structure calculations. Phys Rev B 74(8):081201. doi:10.1103/PhysRevB.74.081201

[52] Yun JN, Zhang ZY, Yan JF, Zhao W, Xu MZ (2015) First-principles study of B or Al-doping effect on the structural, electronic structure and magnetic properties of γ-graphyne. Comput Mater Sci 108:147–152. doi:10.1016/j.commatsci.2015.06.022

[53] Samson S, Fonstad CG (1973) Defect structure and electronic donor levels in stannic oxide crystals. J Appl Phys 44(10):4618–4621. doi:10.1063/1.1662011

[54] Fonstad CG, Rediker RH (1971) Electrical properties of high-quality stannic oxide crystals. J Appl Phys 42(7):2911–2918. doi:10.1063/1.1660648

[55] De Murcia M, Egee M, Fillard JP (1978) Luminescence centers in SnO_2 single crystals. J Phys Chem Solids 39(6):629–635. doi:10.1016/0022-3697(78)90177-4